PNAS RESEARCH ARTICLE | GENETICS

Ablation of lysophosphatidic acid receptor 1 attenuates hypertrophic cardiomyopathy in a mouse model

Anna Axelsson Raja[a,b,1], Hiroko Wakimoto[a,1], Daniel M. DeLaughter[a], Daniel Reichart[a], Joshua Gorham[a], David A. Conner[a], Mingyue Lun[a], Clemens K. Probst[c,d,e], Norihiko Sakai[c,d,e,f], Rachel S. Knipe[c,d,e], Sydney B. Montesi[e], Barry Shea[g], Leonard P. Adam[h], Leslie A. Leinwand[i], William Wan[i], Esther Sue Choi[i], Eric L. Lindberg[j], Giannino Patone[j], Michela Noseda[k], Norbert Hübner[j,l,m], Christine E. Seidman[a,n,o,2], Andrew M. Tager[c,d,e,3], J. G. Seidman[a,2], and Carolyn Y. Ho[n,2]

Contributed by J. G. Seidman; received March 23, 2022; accepted May 25, 2022; reviewed by Elizabeth McNally and Robert Roberts

Myocardial fibrosis is a key pathologic feature of hypertrophic cardiomyopathy (HCM). However, the fibrotic pathways activated by HCM-causing sarcomere protein gene mutations are poorly defined. Because lysophosphatidic acid is a mediator of fibrosis in multiple organs and diseases, we tested the role of the lysophosphatidic acid pathway in HCM. Lysphosphatidic acid receptor 1 (LPAR1), a cell surface receptor, is required for lysophosphatidic acid mediation of fibrosis. We bred HCM mice carrying a pathogenic myosin heavy-chain variant ($403^{+/-}$) with *Lpar1*-ablated mice to create mice carrying both genetic changes ($403^{+/-}$ LPAR1 $^{-/-}$) and assessed development of cardiac hypertrophy and fibrosis. Compared with $403^{+/-}$ LPAR1^{WT}, $403^{+/-}$ LPAR1 $^{-/-}$ mice developed significantly less hypertrophy and fibrosis. Single-nucleus RNA sequencing of left ventricular tissue demonstrated that *Lpar1* was predominantly expressed by lymphatic endothelial cells (LECs) and cardiac fibroblasts. *Lpar1* ablation reduced the population of LECs, confirmed by immunofluorescence staining of the LEC markers Lyve1 and Ccl21a and, by in situ hybridization, for *Reln* and *Ccl21a*. *Lpar1* ablation also altered the distribution of fibroblast cell states. FB1 and FB2 fibroblasts decreased while FB0 and FB3 fibroblasts increased. Our findings indicate that *Lpar1* is expressed predominantly by LECs and fibroblasts in the heart and is required for development of hypertrophy and fibrosis in an HCM mouse model. LPAR1 antagonism, including agents in clinical trials for other fibrotic diseases, may be beneficial for HCM.

hypertrophy | lymphatic endothelial cells | fibroblasts | fibrosis | lysophosphatidic acid receptor

Hypertrophic cardiomyopathy (HCM) is the most common inherited cardiomyopathy (1, 2). Dominantly acting pathogenic variants in genes encoding components of the cardiac sarcomere are an important cause of disease. Variants in cardiac myosin heavy chain (MHC; *MYH7*) cause ∼25% of human HCM (1, 2). In addition to left ventricular hypertrophy (LVH), myocardial fibrosis is a key pathological feature of HCM. Extracellular matrix accumulates up to eightfold more in HCM than in normal hearts and reflects diffuse interstitial fibrosis, focal replacement fibrosis, and perivascular fibrosis (3, 4). Patients with HCM have increased morbidity and mortality compared to the general population due to malignant arrhythmias, heart failure, atrial fibrillation, and stroke (5). Myocardial fibrosis is postulated to be one of the key drivers of these events, and the presence of fibrosis is associated with adverse outcomes (6–11). However, the mechanisms by which sarcomere protein gene mutations induce cardiac fibrosis are largely unknown.

In human studies using cardiac MRI, replacement fibrosis is typically not detectable prior to the development of LVH but increased extracellular volume compatible with interstitial fibrosis has been documented by cardiac MRI in individuals who carry a pathogenic sarcomere mutation but have normal wall thickness (12, 13). Since nonmyocyte cells, including cardiac fibroblasts (FB), do not express the sarcomere genes responsible for causing HCM, the generation of fibrosis is believed to result from activation of cardiac fibroblasts by cardiomyocytes and nonmyocyte cells (14–16). The normal mammalian heart contains five different cardiac fibroblast states distinguishable by RNA expression (17). The origin and type of activating signals are still largely unknown in HCM. Furthermore, we do not know whether the same mechanisms that activate fibroblasts from other organs are the same mechanisms that activate fibroblasts in HCM hearts.

A mouse model of HCM was established by introducing the MHC variant, Arg403Gln, which causes HCM in humans, into the gene that encodes the predominant adult murine cardiac MHC (HCM mice denoted $403^{+/-}$) (18). In $403^{+/-}$ mice, as in human HCM patients, disease pathology develops slowly and is not typically established

Significance

Hypertrophic cardiomyopathy (HCM) is the most common inherited cardiomyopathy. Patients with HCM have increased risk of arrhythmias, heart failure, and stroke. Myocardial fibrosis is a key pathological feature of HCM, but the mechanisms leading to fibrosis are largely unknown. We demonstrate that genetic ablation of the lysophosphatidic acid receptor 1 (LPAR1) reduces hypertrophy and fibrosis in a mouse model of HCM. We track the underlying mechanisms to reduction of lymphatic endothelial cells and altered distribution of fibroblast subtypes. Our findings implicate the LPAR1 pathway in the development of phenotypic HCM. Since the presence of fibrosis is associated with adverse outcomes in HCM, LPAR1 antagonism, being developed for other fibrotic diseases, may also be a promising therapeutic strategy for HCM.

Reviewers: E.M., Northwestern University; and R.R., St Joseph's Hospital and Medical Center.

The authors declare no competing interest.

[1]A.A.R. and H.W. contributed equally to this work.

[2]To whom correspondence may be addressed. Email: cseidman@genetics.med.harvard.edu, seidman@genetics.med.harvard.edu, or cho@bwh.harvard.edu.

[3]Deceased August 11, 2017.

This article contains supporting information online at http://www.pnas.org/lookup/suppl/doi:10.1073/pnas.2204174119/-/DCSupplemental.

Published July 5, 2022.

until age 30 wk (18). Expression of the *MYH7* Arg403Gln variant in cardiomyocytes has been shown to induce proliferation of fibroblast-specific protein 1 (*Fsp1*) expressing nonmyocytes compared with wild-type mice (14). Although transforming growth factor-β (TGF-β) is required for fibrosis development in HCM models with sarcomere gene mutations (14), other relevant fibrosis signaling pathways have not been fully elucidated. Clarifying these signaling pathways is crucial to improving understanding of disease pathogenesis.

Lysophosphatidic acid (LPA) has been shown to stimulate fibrosis in numerous systems, including the heart. Six different LPA receptors (LPAR1 to LPAR6) are encoded in the human and rodent genomes. Previous studies have demonstrated that LPA injection into rats can increase fibrosis postmyocardial infarct and that this LPA response is likely mediated by LPAR3 (19). LPAR1 has been shown to play an important role in the development of fibrosis in several organs, including kidneys, lungs, and skin. Signaling through this 364-amino acid residue G protein-coupled receptor (GPCR) results in fibroblast migration and activation, epithelial cell apoptosis, and vascular leak (20–25). Furthermore, pharmacologic antagonism of LPAR1 has evolved as a promising antifibrotic therapy for a number of fibrotic diseases, including scleroderma and idiopathic pulmonary fibrosis (20, 22–27). However, the role of LPAR1 in the pathogenesis and the development of myocardial fibrosis in HCM is currently undefined.

Because *Lpar1* is expressed at a higher level than other LPA receptors in mouse hearts (Dataset S7), we hypothesized that this receptor might mediate fibrosis in a murine HCM model. This hypothesis was tested by breeding HCM mice ($403^{+/-}$) with mice carrying a deletion in the *Lpar1* gene ($LPAR1^{-/-}$) and analyzing cardiac phenotypes and gene expression in the resulting HCM mice lacking LPAR1 ($403^{+/-}$ $LPAR1^{-/-}$). The hypertrophic and fibrotic responses in these mice were evaluated by an integrated approach, including standard echocardiography and histological staining together with single-nucleus RNA sequencing (snRNA-seq). snRNA-seq permits the evaluation of cell types (such as cardiomyocytes, fibroblasts, and endothelial cells that express very different genes) and cell states (i.e., subsets of cells within a cell type that express different amounts of the same RNAs). Here, we define both cell type and cell state changes in the LVs of HCM mice lacking LPAR1.

Results

Genetic Ablation of LPAR1 Attenuates the Development of LVH in HCM Caused by a Pathogenic MHC Variant. The in vivo consequences of LPAR1 ablation on the development of LVH and secondary structural changes in HCM mice were assessed noninvasively by serial echocardiography. As in human HCM patients, disease pathology develops slowly in $403^{+/-}$ mice. Myocardial hypertrophy and fibrosis are absent in 6-wk-old mice, variably present at 15 wk, and established at 30 wk (18). The $403^{+/-}$ $LPAR1^{-/-}$ mice exhibited significantly less LVH than $403^{+/-}$ $LPAR1^{WT}$ starting from 12 wk of age (Fig. 1) and LVH remained significantly less after accounting for the smaller body size of the $403^{+/-}$ $LPAR1^{-/-}$ mice. By 42 wk of age, when LVH was fully developed in $403^{+/-}$ $LPAR1^{WT}$ mice, LV wall thickness remained largely unchanged from baseline in $403^{+/-}$ $LPAR1^{-/-}$ mice (maximal posterior LV wall thickness 1.05 ± 0.22 mm for $403^{+/-}$ $LPAR1^{WT}$ vs. 0.71 ± 0.13 mm for $403^{+/-}$ $LPAR1^{-/-}$, $P < 0.001$) (Table 1). Maximal LV posterior wall thickness in $403^{+/-}$ $LPAR1^{-/-}$ mice was comparable to wild-type mice (Dataset S1). Ablation of only one copy of *Lpar1* ($403^{+/-}$ $LPAR1^{+/-}$) did not attenuate the development of LVH (Dataset S1). In multivariable linear regression analysis including age, body surface area (BSA), and genotype, *Lpar1*-genotype emerged as the only significant predictor of LV posterior wall thickness. Cardiac morphology of $LPA^{-/-}$ mice, without the MHC Arg403Gln mutation ($MHC^{WT}/LPAR1^{-/-}$), was indistinguishable from that of wild-type mice as assessed by echocardiography (Fig. 1).

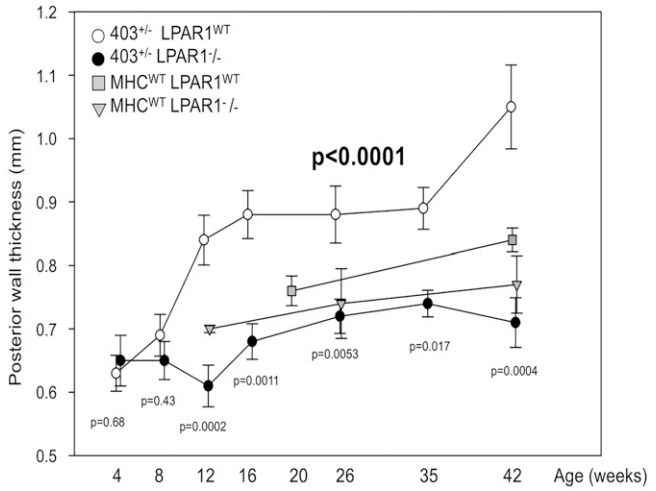

Fig. 1. HCM mice lacking LPAR1 do not develop LVH. LV wall thickness, assessed by echocardiography, of $403^{+/-}$ $LPAR1^{-/-}$ mice (black) and $403^{+/-}$ $LPAR1^{WT}$ (white), age 4 to 42 wk (n = 22). Mixed-models analysis for repeated measures demonstrated a significant difference between the development of posterior wall thickness for $403^{+/-}$ $LPAR1^{-/-}$ mice (black) and $403^{+/-}$ $LPAR1^{WT}$ (white) over time ($P < 0.0001$ for interaction with group and time). Likelihood of LVWT differences occurring by chance at 8, 12, 16, 26, and 42 wk (P values) were also assessed by t tests for differences between $403^{+/-}$ $LPAR1^{-/-}$ and $403^{+/-}$ $LPAR1^{WT}$ mice.

Genetic Ablation of LPAR1 Attenuates Myocardial Fibrosis in HCM Mice. HCM mice generally begin to develop fibrosis by age 15 wk and cardiac fibrosis is well-established by age 30 wk. To examine whether LPAR1-ablation alters development of myocardial fibrosis, male mice were killed at an advanced age (>52 wk) to allow quantification of cardiac fibrosis and collagen content.

By 52 to 66 wk of age, $403^{+/-}$ $LPAR^{-/-}$ hearts displayed significantly less fibrosis than $403^{+/-}$ $LPAR1^{WT}$ hearts as assessed by Masson's trichrome staining (median 2.1 vs. 4.8% of LV mass $P = 0.04$) (Fig. 2 *A* and *C*). The amount of fibrosis in $403^{+/-}$ $LPAR1^{-/-}$ cardiac tissue was indistinguishable from wild-type mice (median 2.1 vs. 1.8% of LV, $P = 0.98$). In addition, myocardial collagen content was significantly lower in $403^{+/-}$ $LPAR1^{-/-}$ as compared to $403^{+/-}$ $LPAR1^{WT}$ as assessed by both Sirius red staining (median 1.7 vs. 5.2% of LV, $P = 0.04$) (Fig. 2 *B* and *D*) and hydroxyproline content (median 18.3 vs. 49.9 mcg/mL, $P = 0.004$) (Fig. 2*E*). These results indicate that LPAR1 is necessary for the development of myocardial fibrosis in HCM mice.

LPAR1 Ablation Was Associated with Reduced Numbers of *Fsp1*-Expressing Cells. The $403^{+/-}$ mouse hearts contain approximately fourfold more FSP1-expressing nonmyocytes than wild-type hearts (14). To test the hypothesis that reduced fibrosis in $403^{+/-}$ $LPAR1^{-/-}$ reflected a reduced number of *Fsp1*-expressing fibroblasts, we counted cells stained with antibodies to FSP1. There were significantly fewer *Fsp1*-expressing cells in $403^{+/-}$ $LPAR1^{-/-}$ cardiac tissue than in $403^{+/-}$ $LPAR1^{WT}$ cardiac tissue

Table 1. Echocardiographic measurements in male mice at 42 wk of age

	$403^{+/-}$ $LPAR1^{WT}$ ($n = 12$)	$403^{+/-}$ $LPAR1^{-/-}$ ($n = 10$)	P
Age (wk)	41 ± 3	43 ± 5	0.36
SBP (mmHg, $n = 6$)	129 ± 4	129 ± 5	0.92
IVSd (mm)	0.90 ± 0.13	0.74 ± 0.13	<0.001
LVPWd (mm)	1.05 ± 0.22	0.71 ± 0.13	<0.001
LVIDd (mm)	3.38 ± 0.21	2.99 ± 0.35	<0.001
LVIDs (mm)	1.66 ± 0.38	1.53 ± 0.35	0.41
FS (%)	51 ± 9	49 ± 8	0.58
LAd (mm)	2.34 ± 0.25	1.81 ± 0.14	<0.0001

Results are presented as mean ± SD. FS, fractional shortening; IVSd, intraventricular septum in diastole; LAd, left atrial diameter; LVIDd, left ventricular internal diameter in diastole; LVIDs, left ventricular internal diameter in systole; LVPWd, left ventricular posterior wall in diastole; SBP, systolic blood pressure.

(median 92 vs. 152 *Fsp1*-expressing cells per mouse, $P = 0.025$; ($n = 3$ to 5 animals per group, one section per animal) (Fig. 3). Previous studies demonstrated that while *Fsp1*-expressing nonmyocyte cells proliferate in HCM mouse hearts, *α-SMA*–expressing fibroblasts do not (14).

Cardiomyocyte Disarray in $403^{+/-}$ Hearts Is Not Affected by Ablation of LPAR1. Cardiomyocyte disarray is another characteristic histopathological feature of HCM. To determine whether LPAR1 ablation affects disarray, the orientation of myofibrils was assessed in cardiac tissue sections from five mice (total 50 segments per mouse) (*SI Appendix*, Fig. S1). In contrast to the effects on hypertrophy and fibrosis, we found no significant difference in myofibril alignment in $403^{+/-}$ $LPAR1^{-/-}$ as compared to $403^{+/-}$ $LPAR1^{WT}$ (per animal [$P = 0.79$], per slides [$P = 0.68$], and per all segments [$P = 0.70$]).

snRNA-seq Demonstrates that Lpar1 RNA Is Expressed in Multiple Cell Types. To further characterize the effect of LPAR1 ablation, RNA expression was assessed in $403^{+/-}$ $LPAR1^{-/-}$ and $403^{+/-}$ $LPAR1^{WT}$ hearts. Bulk RNA-seq analyses of total mRNA was initially performed. RNA expression in $403^{+/-}$ $LPAR1^{-/-}$ and $403^{+/-}$ $LPAR1^{WT}$ was virtually indistinguishable (Dataset S2) ($n = 3$ hearts per group). *Lpar1* mRNA levels in $403^{+/-}$ $LPAR1^{WT}$ and $403^{+/-}$ $LPAR1^{-/-}$ hearts were also similar (Dataset S2) (*Lpar1* levels in $403^{+/-}$ $LPAR1^{WT}$ and $403^{+/-}$ $LPAR1^{-/-}$ hearts were 4.3 vs. 3.7 reads per kilobase and million mapped reads; $P = 0.87$), suggesting the mutationally altered RNA was not subject to nonsense-mediated decay. However, evaluation of bulk RNA-seq reads confirmed that *Lpar1* mRNA in $403^{+/-}$ $LPAR1^{-/-}$ mouse hearts lacked exon 3, which encodes 252 amino acids, as expected. The residual *Lpar1* mRNA is predicted to encode a nonfunctional 12-amino acid protein.

We postulated that although bulk RNA-seq could not identify significant differences in RNA expression between LPAR1-null LV and wild-type LV, the significant morphologic differences between these hearts would be reflected in RNA expression changes in specific cardiac cell populations. Therefore, to improve resolution, we performed snRNA-seq to assess gene expression in LV tissue (MHC^{WT} $LPAR1^{-/-}$, 9,430 nuclei; $403^{+/-}$ $LPAR1^{-/-}$, 8,372 nuclei; $403^{+/-}$ $LPAR1^{WT}$, 7,920 nuclei; MHC^{WT} $LPAR1^{WT}$, 12,808 nuclei). Unbiased clustering of the global object from a total of 38,530 nuclei identified 10 distinct clusters, termed cell types, among the 38,530 nuclei (*Materials and Methods*, Fig. 4, *SI Appendix*, Figs. S2–S4, and Datasets S3 and S4). Annotation of the 10 clusters based on marker genes and differentially expressed genes allowed identification of 10 major cell types, including cardiomyocytes, endocardial cells, endothelial cells, epithelial cells, fibroblasts, lymphatic endothelial cells (LECs), macrophages, pericytes, smooth muscle cells, and lymphocytes (Fig. 4*A*). *Lpar1* expression was highest in fibroblasts (~4 normalized reads per nucleus), LECs (~1 normalized read per nucleus), and endothelial cells (~0.5 normalized reads per nucleus) (Fig. 4*B* and Dataset S5). Myocytes demonstrated scant *Lpar1* expression (~0.03 normalized reads per nucleus). In cardiomyocytes, *Tgfb* (*1*, *2*, or *3*) and *Lpar1* were expressed in the same cell less than expected by chance ($P = 0.01$), whereas in fibroblasts, *Tgfb* (*1*, *2*, or *3*) and *Lpar1* were expressed in the same cell ($P < 0.008$) (Dataset S5).

Ablation of LPAR1 Is Associated with Reduction of the Lymphatic Endothelial Expressed *Reln* and *Ccl21a* and Altered Fibroblast Cell State Distribution. The distribution of most cell types was not significantly altered in LPAR1-deficient hearts compared to normal mouse hearts (Dataset S3) (fold-change < 2 in both non-HCM mice and HCM mice). However, one cell type, LECs, was greater than fourfold reduced in LPAR1-deficient hearts (Dataset S3). Although 738 genes were expressed at significantly ($P < 0.05$ corrected for multiple testing of 30,000 genes) higher or lower levels than in other LV cells, the two most distinguishing marker genes for the population of LECs were *Reln* (reelin) and *Ccl21a* (Chemokine [C-C motif] ligand 21). Both *Ccl21a* and *Reln* were expressed at least eightfold higher in LECs than in any other cell type as measured by snRNA-seq (Dataset S5). Because LymphEC represent ~1% of the nuclei in the wild-type mouse heart (Dataset S3), neither *Reln* nor *Ccl21a* are likely to be expressed sufficiently in the entire heart to be detected by bulk RNA-seq (Dataset S2). To confirm the reduced number of LECs expressing these genes in LPAR1-deficient hearts we identified: 1) *Ccl21a* expressing cells by immunohistochemistry and localized them to LECs (LYVE1 antibody) (Fig. 5) ($403^{+/-}$ $LPAR1^{-/-}$ [$n = 5$] and $403^{+/-}$ $LPAR1^{WT}$ [$n = 3$], one section per animal) and 2) *Reln* expressing cells by in situ hybridization with a fluorescent-labeled RELN probe (Fig. 6) (RNAscope©, $403^{+/-}$ $LPAR1^{-/-}$ [$n = 3$] and $403^{+/-}$ $LPAR1^{WT}$ [$n = 3$], one section per animal). *Reln*-hybridizing cells were observed both in $LPAR1^{-/-}$ hearts and in $LPAR1^{WT}$ hearts near small vessels (Fig. 6). The intensity (number of hybridization speckles per cell) (Fig. 6*B*) were similar in $LPAR1^{-/-}$ and $LPAR1^{WT}$ hearts. However, the number of *Reln*-hybridizing cells were ~3× reduced ($P = 2.1e\text{-}4$) (Fig. 6*C*) in $LPAR1^{-/-}$ hearts compared to $LPAR1^{WT}$ hearts.

In addition to defining the distribution of cell types, snRNA-seq also defines the distribution of cell states (subsets of cells within a cell type that express different amounts of the same RNAs). Given the decreased fibrosis observed in $403^{+/-}$ $LPAR1^{-/-}$ mice (Fig. 2), we hypothesized that the distribution

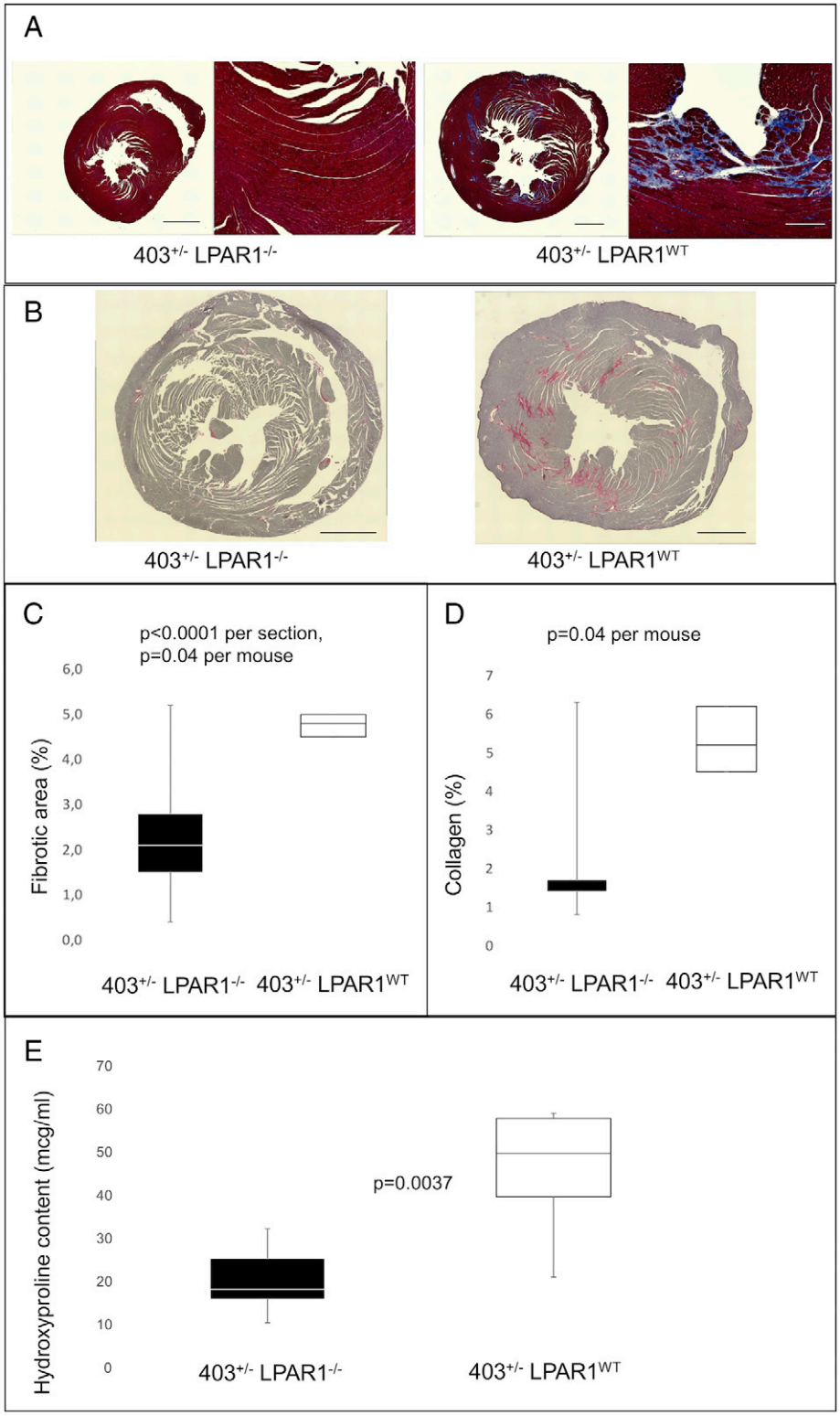

Fig. 2. HCM mice lacking LPAR1 develop significantly less cardiac fibrosis than HCM mice with LPAR1. (*A*) Representative transverse sections and details of the LV from 52-wk-old mice stained with Masson's trichrome (*Left*) $403^{+/-}$ $LPAR1^{-/-}$; (*Right*) $403^{+/-}$ $LPAR1^{WT}$. (Scale bars, 1 mm for black bar, 200 μm for yellow bar.) Fibrotic area was assessed using the BZ-II Analyzer software (Keyence) from images taken with 10× objective lens (BZ-9000, Keyence). (*B*) Representative transverse sections and details of the LV from 52-wk-old mice stained with Sirius red (*Left*) $403^{+/-}$ $LPAR1^{-/-}$, (*Right*) $403^{+/-}$ $LPAR1^{WT}$. (Scale bars, 1 mm.) Collagen fibers were assessed using the BZ-II Analyzer software (Keyence) from images taken with 10× objective lens (BZ-9000, Keyence). (*C*) Reduction in fibrotic area in $403^{+/-}$ $LPAR1^{-/-}$ mice assessed by Masson-trichrome staining in at least eight sections per mouse (n = 3 to 5 per group, age 52 to 66 wk). Results expressed as median and interquartile range. Note box-and-whisker plots: when the interquartile value and the range are indistinguishable no whisker is visible (*C* and *D*). Between group differences were evaluated using Student's t-test. (*D*) Reduction in collagen in $403^{+/-}$ $LPAR1^{-/-}$ mice assessed by Sirius red staining in four to seven sections per mouse (n = 3 to 5 per group, age 52 to 66 wk). Results expressed as median and interquartile range. (*E*) Biochemical analysis of fibrosis shows reduced hydroxyproline content in cardiac tissue of $403^{+/-}$ $LPAR1^{-/-}$ mice (n = 6 per group, age 52 to 66 wk). Results expressed as median and interquartile range. Between-group differences were evaluated using Student's t-test.

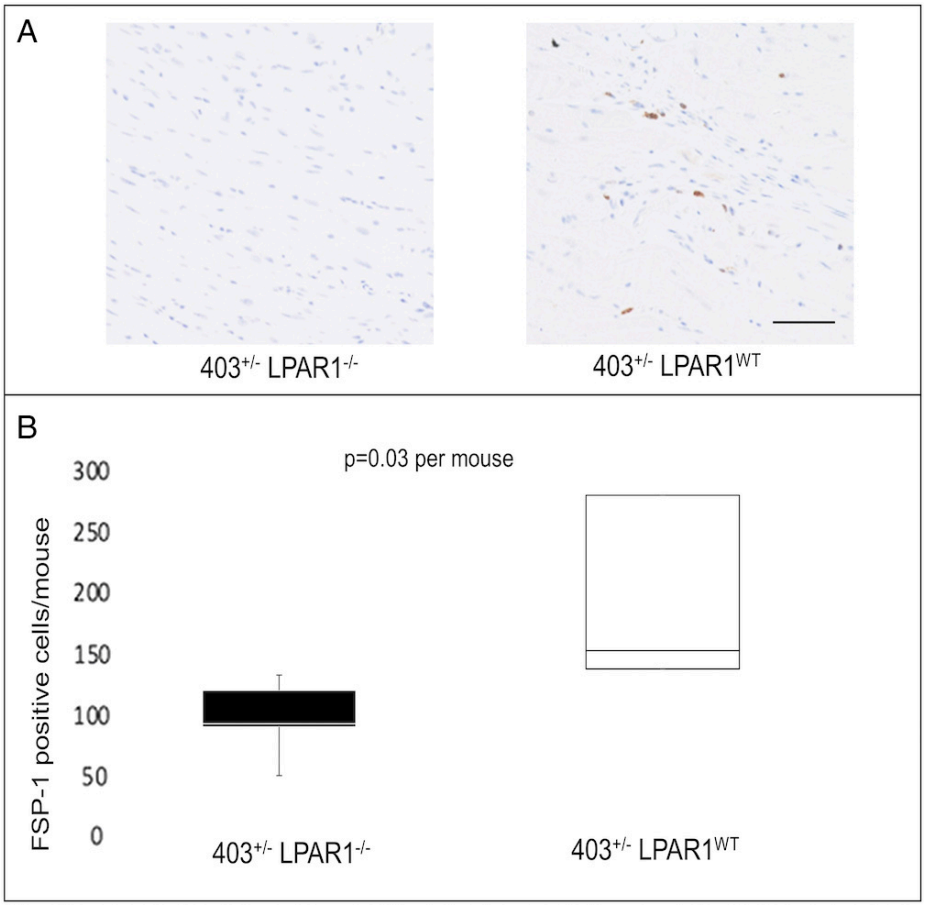

Fig. 3. Accumulation of FSP1-expressing nonmyocytes was reduced in $403^{+/-}$ $LPAR1^{-/-}$ mice compared to $403^{+/-}$ $LPAR1^{WT}$. (*A*) Representative sections of the LV from 50-wk-old mice stained for FSP1. (Scale bar, 20 μm.) (*B*) FSP-1^{+} cells were significantly lower in $403^{+/-}$ LPAR1 $^{-/-}$ cardiac tissue than in $403^{+/-}$ $LPAR1^{WT}$ cardiac tissue (n = 3 to 5 animals per group). Results expressed as median and interquartile range. Note box-and-whisker plots: when the interquartile value and the range are indistinguishable no whisker is visible. Between-group differences were evaluated using Student's t-test.

of fibroblast cell states would be different in hearts with and without functional *Lpar1* mRNA. To define fibroblast cell states, all fibroblasts from both wild-type and LPAR1-deficient hearts were reclustered, replotted, reharmonized, and single nuclei were compared. Five different fibroblast cell states (FB0 to FB4) (Fig. 7 and Dataset S3) were identified. More than 500 differentially expressed genes were identified (Dataset S4).

To systematically assess the role of each fibroblast state we performed gene ontology pathway analyses using cell-state enriched marker genes (Table 2 and Datasets S4 and S6). RNAs encoding proteins in nine nonredundant signaling pathways were enriched in FB0 and FB1 fibroblasts compared to other fibroblast cell states (Table 2 and Dataset S6). In general, the TGF-β signaling pathways were more strongly activated in FB0, while the actin cytoskeletal remodeling RhoGTPase signaling pathway is enhanced in FB1 cells (Table 2 and Dataset S6). The actin-cytoskeletal remodeling RhoGTPase pathway mediates cell motility and proliferation (28), while the TGF-β pathway is involved primarily in production of extracellular matrix associated with scar formation (29). Furthermore, the TGF-β pathway in FB0 cells induces collagen genes *Col1a1* and *Col4a3*, presumably the RhoGTPase pathway activates *Col4a1* in FB1 cells. This shift in collagen gene expression may be secondary to changes in *Tgfb2* gene expression found in these cell states and is presumably related to the reduction of thrombospondin (THBS2) and a tissue inhibitor of a metalloprotease (TIMP2). Although we have not defined the precise mechanism by which reduction in LPA signaling mediates changes in extracellular matrix, these analyses provide strong circumstantial evidence that these changes are mediated through two different cell types: LECs and fibroblast states 0 and 1.

Further evidence for differences in cell-state function comes from identification of particular differentially expressed genes. For example, *Mfap5* (microfibrillar-associated protein 5), which has been associated with fibrosis in other organs (30), is expressed two- to fourfold higher in FB0 and FB3 cell states than in other fibroblast cell states (Fig. 7 and Dataset S5). *Fap* (fibroblast activation protein) is increased in FB1 fibroblasts (Fig. 7 and Dataset S5). We found that more FB1 and FB2 fibroblasts are present in hearts with normal amounts of LPAR1 and fewer in hearts lacking LPAR1, regardless of αMHC^{403} genotype (+/− or WT) expressed (Dataset S3); conversely more FB0 and FB3 fibroblasts are expressed in hearts lacking LPAR1 than hearts with LPAR1.

Human (Normal and HCM) *LPAR* Gene, *RELN*, and *CCL21* Expression. Expression of the six *LPAR* receptors, *RELN*, and *CCL21* genes in mouse and human HCM and "control" LV (Datasets S7 and S8) were measured by snRNA-seq. The patterns of LPAR genes in each cell type are highly conserved between mouse and human (normal and HCM) LV tissue. That is, *LPAR1* is expressed most abundantly in fibroblasts and LECs, while *LPAR6* is expressed primarily in other endothelial cells. Furthermore, LPAR gene expression is similar in HCM and "normal" LV cells. Male and female (human) hearts contain similar amounts of *LPAR* RNAs (Dataset S9).

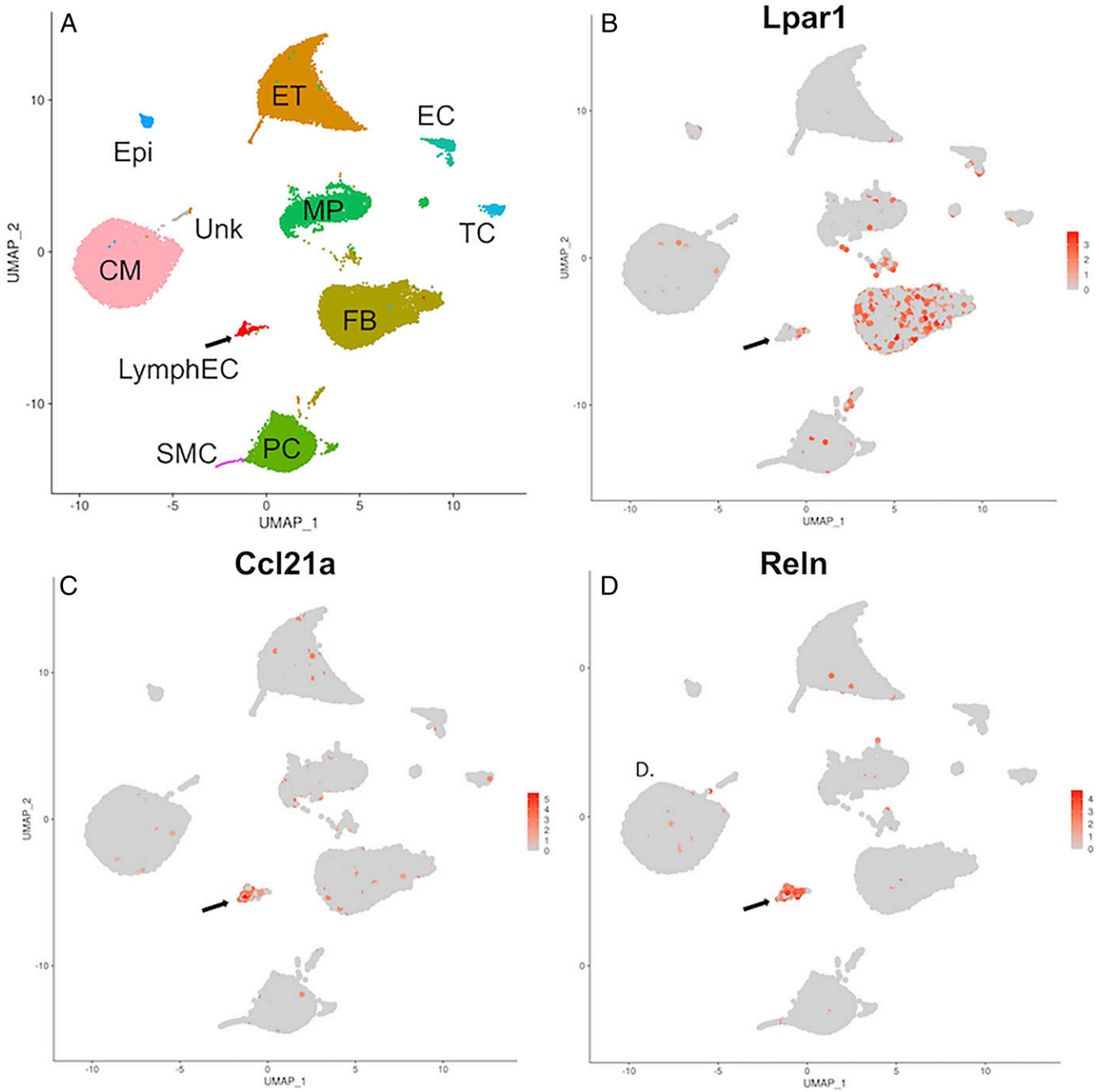

Fig. 4. snRNA-seq of LV tissue identifies 10 distinct cell types. UMAP plots derived from RNA-seq of single nuclei isolated from the LVs of $403^{+/-}$ $LPAR1^{-/-}$, $403^{+/-}$ $LPAR1^{WT}$, MHC^{WT} $LPAR1^{-/-}$, and MHC^{WT} $LPAR1^{WT}$ mice. RNA-seq of single nuclei isolated from the LVs of different genotypes mice were compared to one another after applying UMAP and other harmonization procedures. (*A*) UMAP plot labeled with cell type assigned based on expression of marker genes (Dataset S4). Ten distinct cell types are identified, including: cardiomyocytes (CM); endocardial cells (EC), endothelial cells (ET); epithelial cells (Epi); fibroblasts (FB); lymphatic endothelial cells (LymphEC; indicated with an arrow); macrophages (MP); pericytes (PC); smooth muscle cells (SMC); lymphocytes (TC). (*B–D*) UMAP plots overlaid with the expression of *Lpar1* (*B*), *Ccl21a* (*C*) and *Reln* (*D*). *Lpar1* expression is most abundant in fibroblasts. *Ccl21a* and *Reln* are marker genes for LymphEC.

As in mouse HCM hearts, human HCM hearts contain less *RELN* and *CCL21* RNA than control hearts (Dataset S8). Human HCM LV express 74% of control *RELN* RNA levels and 20% of control *CCL21* RNA levels ($P = 0.02$).

Discussion

The LPAR1-mediated signaling pathway has been shown to mediate fibrosis in lungs, skin, kidney, and liver (20, 22–25), but its role in cardiac fibrosis is not well characterized. Therefore, we investigated this pathway in HCM, a prototypical fibrotic disorder of the heart, where cardiac fibrosis is prevalent in both human patients and mouse models. By studying genetically modified mice that both carry a pathogenic MHC variant that causes HCM and lack LPAR1, we demonstrate that genetic ablation of LPAR1 significantly attenuated phenotypic evolution of HCM. Compared with HCM mice with intact LPAR1 ($403^{+/-}$ $LPAR1^{WT}$), HCM mice with LPAR1 ablated ($403^{+/-}$ $LPAR1^{-/-}$) had marked reduction of LVH and myocardial fibrosis, pathognomonic features of this disease.

The secreted bioactive LPA activates fibroblasts and other cells via binding to its receptor, LPAR1. Previous studies have

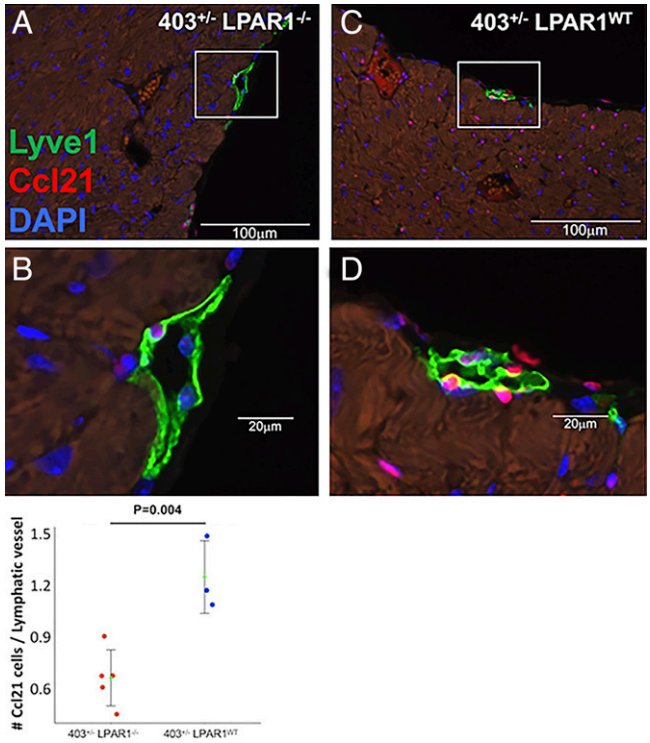

Fig. 5. LV sections from $403^{+/-}$ $LPAR1^{-/-}$ (*A* and *B*) and $403^{+/-}$ $LPAR1^{WT}$ (*C* and *D*) hearts stained with LYVE1 (lymphatic endothelium), CCL21, and DAPI. *B* and *D* are enlarged regions (boxed) from *A* and *C*, respectively. Number of $CCL21a^{+}$ cells per lymphatic vessels was counted from entire section of $403^{+/-}$ $LPAR1^{-/-}$ and $403^{+/-}$ $LPAR1^{WT}$ heart (n = 5 and 3, respectively, one section per animal).

demonstrated different mechanisms underlying the effect of LPAR1 deletion in other organs. In the lungs, LPA exhibits a chemoattractant activity, promoting fibroblast migration into injured tissue. Genetic ablation or pharmacologic antagonism of LPAR1 ameliorates progression of pulmonary fibrosis by attenuating fibroblast migration and activation, epithelial cell apoptosis, and vascular leak (20). In scleroderma, LPAR1 ablation has been shown to reduce dermal thickness and collagen deposition by reducing myofibroblast accumulation and by abrogating TGF-β signaling pathways (23). Studies in models of renal fibrosis indicate that LPAR1 signaling indirectly induces renal fibrosis by connective tissue growth factor (CTGF)-mediated fibroblast proliferation and differentiation. *CTGF* was primarily expressed by tubular epithelial cells, indicating that interactions between epithelial cells and fibroblasts play an essential role in the development of renal fibrosis (22, 24). Thus, LPAR1 is required for the development of fibrosis in different organs across a variety of different stimuli. In addition, LPA has also been shown to induce hypertrophy of cardiomyocytes by different pathways than conventional GPCR activation (19, 31). In a rat model of myocardial infarction and in patients with myocardial infarction, serum concentration of LPA and expression of *LPAR1* has been shown to be elevated, suggesting that LPA is involved in the pathophysiology (19, 32, 33). Notably in this study, we demonstrate that much of the fibrotic response to LPA is mediated via LPAR1. We have previously demonstrated that TGF-β is also required to mount a fibrotic response to this mutation. In the present study we observed that, in fibroblasts, *Tgfb* (*1*, *2*, or *3*) and *Lpar1* were expressed in the same cell more than expected by chance. Whether these two signaling pathways act independently or in concert will be addressed in future studies.

Our findings in a mouse model of HCM indicate that LPAR1 is necessary for fibroblast accumulation in myocardial fibrosis. As with the mouse model of bleomycin-induced lung injury (20), LPAR1 ablation in HCM mice reduced the number of fibroblasts expressing *Fsp1* in LV tissue, suggesting that decreased recruitment or proliferation of fibroblasts contributes to the reduced fibrosis seen in LPAR1-deficient HCM mice. snRNA-seq demonstrated that in the heart, *Lpar1* is predominantly expressed by fibroblasts, LECs, macrophages, and endothelial cells, not cardiomyocytes. Ablation of LPAR1 was associated with specific reduction of the LECs, defined by marker genes, including reelin (encoded by *Reln*) and chemokine *Ccl21a*. This cell population and associated proteins have not been well-characterized in cardiac fibrosis or HCM, although reelin has been identified as playing a role in cardiac development (34), and both reelin and CCL21 have been implicated in liver and kidney fibrosis.

Reelin is an extracellular matrix protein that is up-regulated in the fibrotic liver, particularly in response to liver injury, and expression appears to correlate with the stage of liver fibrosis (35–38). Most recently, reelin has been associated with enhancing vascular inflammation and arterial thrombosis by promoting platelet activation and thrombus formation (38).

Chronic liver disease has also been associated with expansion of liver LECs and increased expression of *CCL21* (39). CCL21 has also been shown to promote fibrogenesis related to chronic hepatitis C and chronic heart failure (40, 41). In renal fibrosis, CCL21 has been shown to be a chemoattractant for CCR7-expressing dendritic cells, lymphocytes, and fibrocytes. Inhibition of CCR7-CCL21 signaling pathways reduced infiltration of those cells and fibrosis (42, 43). Our finding that *Ccl21a* and *Reln* are coexpressed in LECs may provide useful insights for developing biomarkers of fibrotic disease. Although additional work is needed to determine how these changes relate to the pathogenesis of HCM, given that LPAR1 is a cell surface receptor and given that fibroblasts and LECs express the highest levels of LPAR1 of all cardiac cells, we speculate that LPA is mediating its effect through this receptor found on the surfaces of these cells. Overall, our findings suggest that the reduction of the LECs, associated with LPAR1 ablation in the HCM mouse model, is at least in part responsible for the observed reduction in myocardial fibrosis.

In addition to the effect of LPAR1 ablation on reducing the population of LECs, LPAR1 ablation altered gene expression in fibroblasts and changed the distribution of fibroblast subtypes or cell states. Ablation of LPAR1 was associated with a decrease in the number of FB1 and FB2 fibroblasts and increase in FB0 and FB3 fibroblasts. Pathway analyses of marker genes that define these cell states show that FB0 and FB1 express high levels of genes involved in TGF-β signaling (Table 2 and Dataset S6). Consistent with the hypothesis that TGF-β signaling and lysophosphatidic pathways interact to modulate fibrosis in the heart. Defining genes that are differentially expressed between fibroblast cell states FB1 and FB2 in LPAR1 wild-type hearts versus FB0 and FB3 in LPAR1-deficient hearts may provide insights into how LPAR1 contributes to myocardial fibrosis and further define the role of myocardial fibrosis in the pathogenesis of HCM. For example, *Fap* is increased in FB1 and FB2 fibroblasts. While an increase in FAP alone in $403^{+/-}$ $LPAR1^{WT}$ hearts is unlikely to fully explain fibroblast proliferation in HCM, targeting the protein and the cells that express it with chimeric antigen receptor T cells (CAR-T) have been shown to reduce fibrosis in other mouse models of cardiac disease (44, 45). Future experiments targeting FB1 and FB2 cells with CAR-T cells will help distinguish the role of these cells in

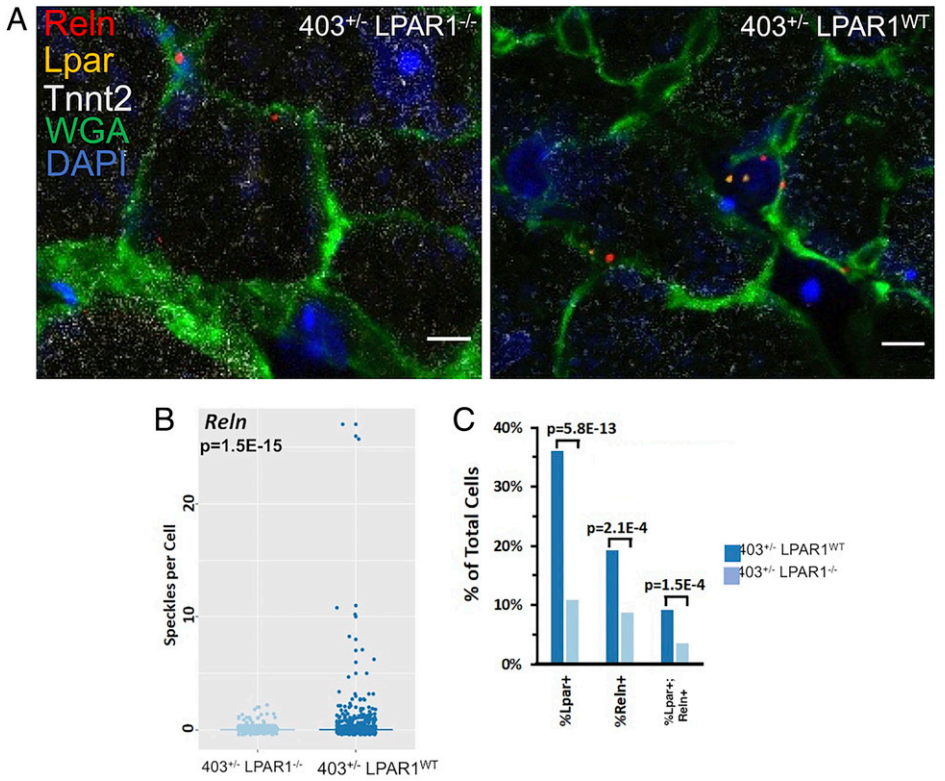

Fig. 6. *Reln* transcripts, detected by RNA in situ hybridization, are decreased in $403^{+/-}$ $LPA1^{-/-}$ LV cells compared to $403^{+/-}$ $LPA1^{WT}$. (*A*) Representative photomicrographs of $403^{+/-}$ $LPAR^{-/-}$ and $403^{+/-}$ $LPAR^{WT}$ LV sections hybridized to *Lpar1* (orange), *Reln* (red), DAPI (dark blue), *Tnnt2* (light blue) in situ hybridization (RNAScope) probes. Sections are displayed with cell boundaries stained with wheat germ agglutinin (WGA, green) and without WGA (no cell boundaries) (*Materials and Methods*). (Scale bars, 5 μM.) (*B*) *Reln*-expressing cells (e.g., LymphEC) were identified in in situ immunofluorescent images using image processing software (Cell Profiler) to count speckles corresponding to immunofluorescent probe signal per cell. The number of hybridization "speckles" visualized using *Reln* probe plotted per cell per genotype. Each dot represents one cell. (*C*) Plot of the percent of all cells counted in $403^{+/-}$ $LPA1^{WT}$ (n = 9 images, 514 cells overall) or $403^{+/-}$ $LPA1^{WT}$ (n = 6 images, 229 cells overall) sections positive for *Lpar1*, *Reln*, or both probes. *P* values calculated using Fisher's exact test.

HCM hearts. While the molecular mechanism by which the activated LPAR1 receptor transmits its signal to the nucleus and activates changes in RNA expression remains uncertain, we demonstrate that in the absence of LPAR1 a significant fraction of FB0 and FB3 cells shift to the FB1/FB2 cell pattern of gene expression. Whether this shift in the fibroblast cell-state distribution is required to mediate HCM-phenotypes remains uncertain.

Our study has several limitations. The studies presented here demonstrate that Lpar1-mediated signaling is required for the pathophysiologic response, including the development of fibrosis, to an HCM-causing mutation. However, the mechanism by which an HCM-causing mutation, which is expressed in a cardiomyocyte, transmits its signal to LECs and fibroblasts, where LPAR1 is expressed at highest levels remains unknown. Indeed, it is possible that differential activation of the LPAR1-mediated signaling pathway by different disease-causing genes (e.g., HCM caused by troponin T vs. MHC variants) accounts for the different extent of fibrosis and hypertrophy produced in response to pathogenic variation. Furthermore, we do not know whether the lower levels of LPAR1 found on other cell types or states (e.g., macrophages and endothelial cells) also contribute to disease pathology.

Strategies to inhibit LPAR1 are under active exploration as novel treatments for fibrotic disease in humans. A phase II clinical trial of the small-molecule LPAR1 antagonist, BMS-986020, in idiopathic pulmonary fibrosis, demonstrated a reduction in the decline in forced vital capacity at 26 wk (27). A small phase II clinical trial of SAR100842, another LPAR1 antagonist, in diffuse cutaneous systemic sclerosis demonstrated a slightly greater decrease in the modified Rodnan skin score, a measure of skin thickness, with SAR100842 compared to placebo; however, the difference between groups was not statistically significant (26).

In conclusion, our findings provide insights into the mechanisms behind pathological cardiac remodeling in HCM, implicating the LPAR1 pathway in HCM-associated fibrosis. In the LV, *Lpar1* is expressed in distinct populations of LECs and fibroblasts and is required for development of hypertrophy and fibrosis in HCM. LPAR1 ablation attenuates phenotypic evolution of HCM, reduces the population of LECs in the LV, and changes the distribution of fibroblast subtypes. This study highlights an important role of this pathway in driving fibrosis in an additional organ system. Furthermore, there are notable clinical implications as LPAR1 antagonism, being developed for other fibrotic diseases, may also be a promising therapeutic strategy not only for HCM, but potentially for other processes that culminate in myocardial fibrosis.

Materials and Methods

Animals. Two lines of mice, one a model of human HCM carrying a heterozygous missense mutation in the α-cardiac myosin heavy-chain gene (*Myh6*) and the other with homozygous deletion of *Lpar1*, have been previously described (18, 46). We have previously shown that male mice develop phenotypic HCM (LVH and myocardial fibrosis) more consistently than do female littermates (47); thus, for the present study, only male mice were evaluated.

The $403^{+/-}$ mice (mixed 129Sv/J, 129SvEv background) were bred to LPAR1-null mice ($LPAR1^{-/-}$, C57BL/6 background), producing hybrid mice with mixed C57BL/6, 129S6/SvEvTac, 129x1/SvJ genetic background. Second-generation mice carrying both MHC and *Lpar1* mutations ($403^{+/-}$ $LPAR1^{-/-}$) and littermate controls carrying only the *Myh6* missense mutation ($403^{+/-}$ $LPAR1^{WT}$) were used for all studies. $LPAR1^{-/-}$ mice typically have reduced body size; therefore, analyses

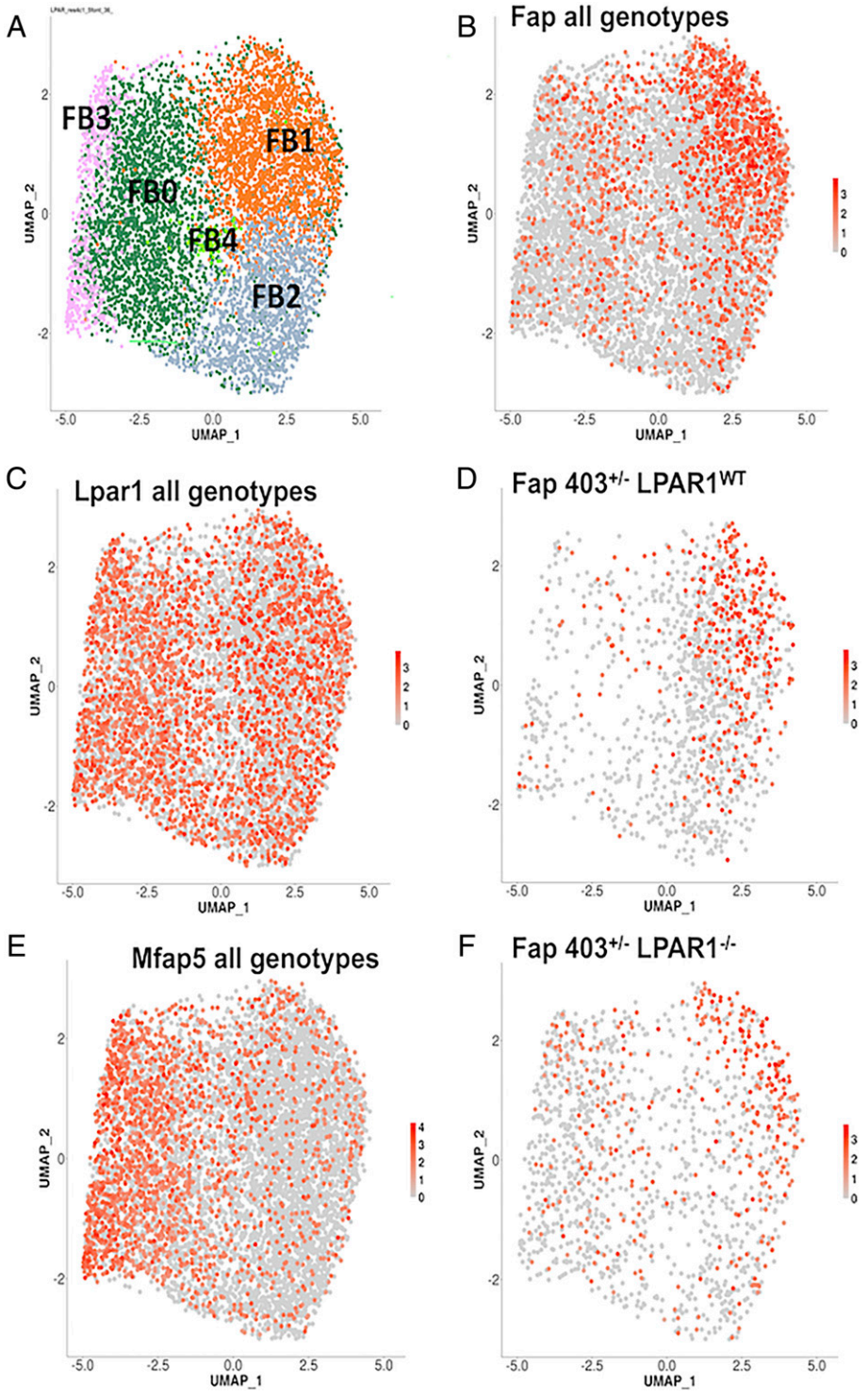

Fig. 7. Fibroblast RNA expression in HCM ($403^{+/-}$) mouse hearts expressing *Lpar1* compared to those lacking *Lpar1*. (*A*) Five fibroblast cell states were defined by reclustering fibroblast nuclei, identified among nuclei made from LVs of $403^{+/-}$ $LPAR1^{-/-}$, $403^{+/-}$ $LPAR1^{WT}$, MHC^{WT} $LPAR1^{-/-}$, and MHC^{WT} $LPAR1^{WT}$ mice. UMAP plots are overlaid with the expression of specified genes in each nucleus. (*B*, *C*, and *E*) Plots contain all nuclei from all genotypes expressing *Fap* (*B*), *Lpar1* (*C*), or *Mfap5* (*E*). *D* and *F* depict only those nuclei with (*D*) or without (*F*) LPAR1.

were adjusted for BSA when appropriate (46). BSA was calculated as weight $(gm)^{2/3} \times 10.5$. Mice were killed after echocardiographic evaluation after reaching full maturity at age 52 wk. All mice were maintained and studied using protocols approved by the Animal Care and Use Committee of Harvard Medical School.

Echocardiography. Serial echocardiography was performed in vivo using Vevo 770 and 2100 (Fujifilm VisualSonics) at ages 4, 8, 12, 16, 26, 35, and 40 wk. Mice were lightly anesthetized under isoflurane vaporizer (VetEquip) in an induction chamber and each limb was placed on the ECG leads on a Vevo Mouse Handling Table (Fujifilm VisualSonics) to maintain body temperature at 37 °C during the study. Anesthesia was discontinued when the mouse had been positioned for imaging and chest hair had been removed with depilatory cream to optimize image quality. All measurements were performed at heart rates between 500 and 550 beats per minute. Two-dimensional (2D) and M-mode images of the LV and left atrium (parasternal long axis and short axis) were obtained. LV chamber dimensions (LV end-diastolic diameter, LV end-systolic diameter, interventricular septal thickness, and LV posterior wall thickness) were averaged from M-mode tracings from three consecutive heart beats and maximal

Table 2. Pathways perturbed in LPAR1-deficient HCM mice identified by fibroblast state marker genes

Rank*	Pathway	Different genes	Total genes	*P* value	FDR	exp_pw_genes
1	Cytoskeleton remodeling. Regulation of actin cytoskeleton organization by the kinase effectors of Rho GTPases	29	58	8.E-15	1.E-11	*Actg1*, *Col1a1*, *Col1a2*, *Col3a1*, *Col4a1*, *Col4a3*, *Col4a4*, *Egfr*, *Erbb4*, *Igfbp4*, *Igf1*, *Ngf*, *Lamb1*, *Lamc1*, *Mme*, *Mmp16*, *Mmp2*, *Msn*, *Nid1*, *Sparc*, *Serpine1*, *Serpine2*, *Sdc2*, *Timp2*, *Timp3*, *Vcan*, *Itga1*, *Itga5*
2	Chemotaxis_Lysophosphatidic acid signaling via GPCRs	40	129	2.E-11	1.E-08	*Actg1*, *Akt3*, *Bcl2*, *Bcl2l1*, *Ctgf*, *Cd36*, *Ctnnb1*, *Diaph1*, *Egfr*, *Ngf*, *Fosl2*, *Foxo1*, *Gnai1*, *Gnao1*, *Gnb4*, *Has2*, *Itga6*, *Itgav*, *Itpr1*, *Itpr2*, *Jun*, *Junb*, *Lpar1*, *Mapk10*, *Mkl1*, *Mkl2*, *Ncor1*, *Stk4*, *Pik3r1*, *Pkn1;Stk3*, *Plcb1*, *Plcb4*, *Plce1*, *Pld1*, *Prkca*, *Prkce*, *Prkch*, *Pkd1*, *Ar*, *Rhobtb1*, *Ar;Rhoj*, *Ar;Rhoq*, *Ar;Rnd3*, *Rock2*, *Slc9a3r2*, *Tcf7l2*, *Tiam1*, *Vcl*, *Taz*
4	TGF-β–induced fibroblast/ myofibroblast migration and extracellular matrix production in asthmatic airways	25	60	9.E-11	3.E-08	*Akt3*, *Bgn*, *Col1a1*, *Col1a2*, *Col3a1*, *Col4a1*, *Col4a3*, *Col4a4*, *Col4a6*, *Col5a1*, *Dcn*, *Fosl2*, *Has2*, *Itga1*, *Itga5*, *Jun*, *Junb*, *Mapk10*, *Mmp2*, *Serpine1*, *Smad3*, *Tgfb2*, *Tgfbr1*, *Tgfbr2*, *Thbs2*, *Timp2*, *Timp3*
5	IL-1β– and Endothelin-1–induced fibroblast/ myofibroblast migration and extracellular matrix production in asthmatic airways	20	40	1.E-10	4.E-08	*Ctgf*, *Col1a1*, *Col1a2*, *Col3a1*, *Col4a1*, *Dcn*, *Ednra*, *Fosl2*, *Has2*, *Il1r1*, *Jun*, *Junb*, *Mmp2*, *Nfkb1*, *Pdgfra*, *Pdgfrb*, *Serpine1*, *Timp3*, *Vcan*
6	Transcription_HIF-1 targets	32	95	2.E-10	4.E-08	*Abcg2*, *Ak3*, *Arnt*, *Bhlhe40*, *Bhlhe41*, *Bnip3*, *Ctgf*, *Cp*, *Cxcl12*, *Eng*, *Fgf2*, *Flt1*, *Nlk*, *Hif1a*, *Hk2*, *Kitl*, *Lgals1*, *Loxl2*, *Lrp1*, *Mmp2*, *Mxi1*, *Nt5e*, *P4ha1*, *Pgf*, *Rora;Ror1;Ror2*, *Serpine1*, *Slc2a3*, *Stc2*, *Tgfb2*, *Tgm2*, *Vegfa*
7	Cytoskeleton remodeling_Regulation of actin cytoskeleton nucleation and polymerization by Rho GTPases	21	46	4.E-10	8.E-08	*Abi1*, *Actg1*, *Actr3*, *Ar*, *Arpc1b*, *Arpc2*, *Cyfip1*, *Pir*, *Daam1*, *Diaph1*, *Enah*, *Fhod3*, *Fmnl2*, *Gsn*, *Pip5k1b*, *Ar;Rhoj*, *Ar;Rhoq*
8	NF-AT signaling in cardiac hypertrophy	25	65	7.E-10	1.E-07	*Ctgf*, *Col1a1*, *Col1a2*, *Col3a1*, *Col4a1*, *Dcn*, *Ednra*, *Fosl2*, *Has2*, *Il1r1*, *Jun*, *Junb*, *Mmp2*, *Nfkb1*, *Pdgfra*, *Pdgfrb* , *Serpine1*, *Timp3*, *Vcan*
10	Cell adhesion_Integrin-mediated cell adhesion and migration	24	63	2.E-09	3.E-07	*Actg1*, *Actn1*, *Actn2*, *Actn4*, *Arhgef28*, *Col1a1*, *Col1a2*, *Col3a1*, *Col4a1*, *Col4a3*, *Col4a4*, *Col4a6*, *Elmo1*, *Git2*, *Icam1*, *Itga1*, *Itga5*, *Itga6*, *Itgav*, *Lamb1*, *Lamc1*, *Lims1*, *Pard3*, *Parva*, *Parvb*, *Prkca*, *Prkce*, *Prkch*, *Ar*, *Sorbs3*, Syk, *Tiam1*, *Tln2*, *Tns1*, *Vav3*, *Vcam1*, *Vcl*
12	Cell adhesion_ECM remodeling	22	55	3.E-09	4.E-07	*Actg1*, *Col1a1*, *Col1a2*, *Col3a1*, *Col4a1*, *Col4a3*, *Col4a4*, *Egfr*, *Erbb4*, *Igfbp4*, *Igf1*, *Ngf*, *Lamb1*, *Lamc1*, *Mme*, *Mmp16*, *Mmp2*, *Msn*, *Nid1*, *Sparc*, *Serpine1*, *Serpine2*, *Sdc2*, *Timp2*, *Timp3*, *Vcan*, *Itga1*, *Itga5*
15	Development_SLIT-ROBO1 signaling	18	40	9.E-09	9.E-07	*Actg1*, *Akt3*, *Cyth1*, *Cyth3*, *Enah*, *Fli1*, *Slk*, *Lsp1*, *Myh6;Myh7*, *Myh7*, *Myh9*, *Myl2*, *Myl3*, *Pik3r1*, *Ar*, *Robo1*, *Rock2*, *Sh3gl1*, *Slit3*, *Slit2*, *Slit2;Slit3*

FDR, false-discovery rate.
*Pathways were identified.

left atrial dimension was measured antero-posteriorly in the parasternal 2D long-axis view from one cycle. Echocardiographic measurements were performed by an experienced observer blinded to mouse genotype.

Histology. For quantification of fibrosis and collagen, mouse hearts were washed in phosphate buffered saline (PBS) at room temperature and fixed with 4% paraformaldehyde at 4 °C overnight. Paraffin-embedded hearts were sectioned at a thickness of 5 μm to obtain short-axis two-chamber views for minimum eight levels from apex to the base with 100-μm apart between each level and stained using Masson's trichrome and Sirius red. Fibrotic area and collagen fibers (in percent) were assessed using the BZ-II Analyzer software (Keyence) from images taken with 10× objective lens (BZ-9000, Keyence). Areas containing valve tissue were manually excluded.

Hydroxyproline Assay. For quantification of collagen, LV tissue was homogenized in 1 mL of PBS. A 0.5-mL aliquot was digested in 12 N HCl at 110 °C for 12 h. Twenty-five microliter aliquots were desiccated and then resuspended in 0.5 mL of 1.4% chloramine T (Sigma), 10% n-propanol, and 0.5 M sodium

acetate, pH 6.0. After 20 min of incubation at room temperature, 0.5 mL of Erlich's solution (1 M p-dimethylaminobenzaldehyde [Sigma] in 70% n-propanol, 20% perchloric acid) was added and the solution was incubated at 65 °C for 15 min. Absorbance was measured at 550 nm and the amount of hydroxyproline was determined against a standard curve.

Immunocytochemical Analyses. Paraffin-embedded hearts were sectioned at a thickness of 5 μm to obtain short-axis two-chamber views for minimum 8 levels from apex to the base with 100-μm apart between each level. Sections for FSP 1 immunostaining were first treated with xylene for deparaffinization and rehydrated through a graded series of ethanol. Sections were then pretreated with 0.01% trypsin in PBS for 10 min and incubated with 1% BSA for 20 min. Finally, sections were treated with primary rabbit monoclonal antibody to FSP1 overnight, and stained by an Envision kit (Dako). Ten nonoverlapping fields were analyzed for each section by an observer blinded to the mouse genotype.

To identify LECs, immunohistochemical staining with LYVE1 (AF2125, R&D Systems) and CCL21a (PA5-114959, Thermo Fisher Scientific) antibodies were performed using the same methodology.

Myocyte Disarray. Myocyte disarray was assessed as described previously (48, 49). Briefly, the percent disarray was measured using a MATLAB (MathWorks) computer script (49) that identifies the areas of disarray in mouse heart sections stained with Masson trichrome (50).

RNA Expression Analyses by Bulk RNA-seq and snRNA-seq. RNA expression in mouse LV tissue was assessed by both bulk RNA-seq and snRNA-seq. RNA-seq of mouse LV tissue was performed as previously described (48, 51, 52). In summary, LV tissue RNA from 42- to 56-wk-old mice was extracted from excised, PBS-washed homogenized mouse hearts solubilized in TRIzol Reagent (Life Technologies) with TissueLyzer (Qiagen). Preparation of libraries and sequencing has been described in detail previously (51). Nextera fragmented cDNA libraries were constructed from 2 μg total RNA after polyA selection and sequenced on an Illumina HiSeq 2500.

snRNA-seq. snRNA-seq was performed using previously described procedures (51). Single nuclei were obtained from flash-frozen LVs (MHC^{WT} $LPAR1^{-/-}$, 9,430 nuclei; $403^{+/-}$ $LPAR1^{-/-}$, 8,372 nuclei; $403^{+/-}$ $LPAR1^{WT}$, 7,920 nuclei; MHC^{WT} $LPAR1^{WT}$,12,808 nuclei) using mechanical homogenization, as previously described (53, 54). Tissues were homogenized using a 7-mL glass Dounce tissue grinder set (Merck) with 8 to 10 strokes of a loose pestle (A) and tight pestle (B) in homogenization buffer (250 mM Sucrose, 25 mM KCl, 5 mM MgCl2, 10 mM Tris·HCl, 1 mM dithiothreitol [DTT], 1× Protease Inhibitor, 0.4 U/μL RNaseIn, 0.2 U/μL SUPERaseIn, 0.1% Triton X-100 in Nuclease-Free Water). The homogenate was filtered through a 40-μm cell strainer (Corning). After centrifugation (500 × *g*, 5 min, 4 °C) the supernatant was removed and the pellet was resuspended in storage buffer (1× PBS, 4% bovine serum albumin [BSA], 0.2 U/μL Protector RNaseIn). Nuclei were stained with NucBlue Live ReadyProbes Reagents (ThermoFisher) and Hoechst-positive single nuclei were purified by fluorescent activated cell sorting using FACS (Aria, BD Biosciences). Intact nuclei were further fractionated on the Chromium controller (10X Genomics) according to the manufacturer's protocol. Nuclei suspension was adjusted to 400 to 1,000 cells/μL and loaded on the Chromium controller (10X Genomics) with a targeted cell/nuclei recovery of 8,000 per run. 3′ Gene expression libraries were prepared according to the manufacturer's instructions of the v3 Chromium Single Cell Reagent Kits (10X Genomics). After quality control, libraries were sequenced using Nextseq500 (Illumina) with a minimum depth of 20,000 to 30,000 read pairs per nucleus. Scrublet and Solo score was applied to scan for potential doublets. Single nuclei were filtered for counts (300 < nCount_RNA < 8,000), genes (300 < nFeature_RNA <3,500), mitochondrial genes (percent_mito < 1%). Data analysis was conducted using the standard Cell Ranger pipeline. Seurat 3.1 and R 4.0.1 (55). Reads were aligned using Cell Ranger to the mm10 mouse genome. Harmony was used to reduce the contribution of batch, cell alignment rate, number of detected molecules, and mitochondrial gene expression to gene expression measurements (56). Louvain clustering and Uniform Manifold Approximation and Projection (UMAP) visualization were performed for identifying subpopulations and visualization.

RNAscope. Fixed-frozen tissue samples were fixed in 4% paraformaldehyde (ThermoFisher). Sections were cut at 5-μm thickness using a microtome and placed onto SuperFrost Plus slides (VWR). Tissue slides were processed according to manufacturer's instructions (RNAscope Multiplex Fluorescent Assay v1; ACDBio). RNAscope ready- or custom-made target probes were run in parallel to multiplex positive and negative controls. Nuclei were DAPI-stained. Fixed frozen tissue slides were imaged using a LSM710 confocal microscope (Zeiss) and 40× oil-immersion objective (1.3 Oil, DIC III). Channels: DAPI (excitation 375 nm, emission 435 to 480 nm), Alexa Fluor 488 (excitation 492 nm, emission 517 nm), Atto 550 (excitation 560 nm, emission 575 nm), and Atto 647 (excitation 649 nm, emission 662 nm). Visualization and background removal (rolling ball radius) were done using Fiji/ImageJ. Pseudocolors were used to enhance visualization (57).

Statistical Analyses. All analyses were performed by investigators blinded to genotype. Continuous data are presented as mean (±1 SD) or as median (p25 to p75) where appropriate. Unpaired comparisons of continuous variables between genotypes were evaluated using Student's *t*-test, ANOVA, or Mann–Whitney depending on distribution and number of groups. Unpaired comparisons of categorical variables were performed with the χ^2 test. The relationship between ventricular wall thickness and the covariates sex, age and bodyweight, in addition to LPAR1-ablation was analyzed with multivariable linear regression analysis. Comparison of echocardiographic variables were analyzed using a mixed-models analysis for repeated measures. Differentially expressed genes were calculated using the Wilcoxon rank-sum test in snRNA-seq. Bonferroni correction is applied for multiple testing. A two-sided probability of $P < 0.05$ was considered statistically significant. All analyses were performed using SAS v9.2.

Human Control and HCM snRNA-seq. snRNA-seq data for control heart tissues was obtained from the "cellular atlas of the human heart" (17, 54). Explanted heart or myectomy tissues were obtained at the time of surgery, after informed consent was obtained as approved by the Brigham and Women's Institutional Review Board.

Data Availability. Full datasets have been deposited in the Harvard dataverse (https://doi.org/10.7910/DVN/KXPFKK) (58).

ACKNOWLEDGMENTS. This study is an extension of A.M.T.'s seminal research. N.H. is the recipient of a European Research Council advanced grant under the European Union's Horizon 2020 research and innovation program (Grant AdG788970). N.H., C.E.S., and J.G.S. received a grant from the Fondation Leducq and are supported by Grant 2019-202666 from the Chan Zuckerberg Initiative. L.A.L. was supported by NIH GM29090.

Author affiliations: [a]Department of Genetics, Harvard Medical School, Boston, MA 02115; [b]Department of Cardiology, Copenhagen University Hospital Rigshospitalet, 2100 Copenhagen, Denmark; [c]Center for Immunology and Inflammatory Diseases, Massachusetts General Hospital, Harvard Medical School, Boston, MA 02114; [d]Fibrosis Research Center, Massachusetts General Hospital, Harvard Medical School, Boston, MA 02114; [e]Division of Pulmonary and Critical Care Medicine, Massachusetts General Hospital, Harvard Medical School, Boston, MA 02114; [f]Division of Nephrology, Kanazawa University, Kanazawa, 920-1192 Japan; [g]Division of Pulmonary, Critical Care and Sleep Medicine, Albert Medical School of Brown University, Providence, RI 02903; [h]Research and Development, Bristol-Myers Squibb Company, Princeton, NJ 08540; [i]Biofrontiers Institute, Department of Molecular, Cellular, and Developmental Biology, University of Colorado, Boulder, CO 80302; [j]Cardiovascular and Metabolic Sciences, Max Delbrück Center for Molecular Medicine in the Helmholtz Association, 13125 Berlin, Germany; [k]National Heart and Lung Institute, British Heart Foundation Centre of Regenerative Medicine, British Heart Foundation Centre of Research Excellence, Imperial College London, London SW7 2AZ, United Kingdom; [l]Charité-Universitätsmedizin, Berlin Institute of Health, 10117 Berlin, Germany; [m]German Centre for Cardiovascular Research, Partner Site Berlin, 13347 Berlin, Germany; [n]Division of Cardiovascular Medicine, Brigham and Women's Hospital, Boston, MA 02115; and [o]HHMI, Chevy Chase, MD 20815

Author contributions: A.A.R., L.A.L., C.E.S., A.M.T., J.G.S., and C.Y.H. designed research; A.A.R., H.W., D.M.D., D.R., J.G., D.A.C., M.L., C.K.P., N.S., R.S.K., S.B.M., B.S., L.P.A., L.A.L., W.W., E.S.C., E.L.L., G.P., M.N., N.H., A.M.T., J.G.S., and C.Y.H. performed research; A.A.R., H.W., D.M.D., D.R., J.G., D.A.C., C.K.P., N.S., R.S.K., S.B.M., B.S., L.P.A., L.A.L., W.W., E.S.C., E.L.L., G.P., M.N., N.H., C.E.S., A.M.T., J.G.S., and C.Y.H. analyzed data; and A.A.R., H.W., D.M.D., D.R., J.G., D.A.C., M.L., C.K.P., N.S., R.S.K., S.B.M., B.S., L.P.A., L.A.L., W.W., E.S.C., E.L.L., G.P., M.N., N.H., C.E.S., A.M.T., J.G.S., and C.Y.H. wrote the paper.

1. H. Morita *et al.*, Shared genetic causes of cardiac hypertrophy in children and adults. *N. Engl. J. Med.* **358**, 1899–1908 (2008).
2. R. Alcalai, J. G. Seidman, C. E. Seidman, Genetic basis of hypertrophic cardiomyopathy: From bench to the clinics. *J. Cardiovasc. Electrophysiol.* **19**, 104–110 (2008).
3. M. G. St John Sutton, J. T. Lie, K. R. Anderson, P. C. O'Brien, R. L. Frye, Histopathological specificity of hypertrophic obstructive cardiomyopathy. Myocardial fibre disarray and myocardial fibrosis. *Br. Heart J.* **44**, 433–443 (1980).
4. J. Shirani, R. Pick, W. C. Roberts, B. J. Maron, Morphology and significance of the left ventricular collagen network in young patients with hypertrophic cardiomyopathy and sudden cardiac death. *J. Am. Coll. Cardiol.* **35**, 36–44 (2000).
5. C. Y. Ho *et al.*, Genotype and lifetime burden of disease in hypertrophic cardiomyopathy: Insights from the Sarcomeric Human Cardiomyopathy Registry (SHaRe). *Circulation* **138**, 1387–1398 (2018).
6. O. Bruder *et al.*, Myocardial scar visualized by cardiovascular magnetic resonance imaging predicts major adverse events in patients with hypertrophic cardiomyopathy. *J. Am. Coll. Cardiol.* **56**, 875–887 (2010).
7. T. F. Ismail *et al.*, Role of late gadolinium enhancement cardiovascular magnetic resonance in the risk stratification of hypertrophic cardiomyopathy. *Heart* **100**, 1851–1858 (2014).
8. R. H. Chan *et al.*, Prognostic value of quantitative contrast-enhanced cardiovascular magnetic resonance for the evaluation of sudden death risk in patients with hypertrophic cardiomyopathy. *Circulation* **130**, 484–495 (2014).
9. R. Rubinshtein *et al.*, Characteristics and clinical significance of late gadolinium enhancement by contrast-enhanced magnetic resonance imaging in patients with hypertrophic cardiomyopathy. *Circ. Heart Fail.* **3**, 51–58 (2010).
10. R. O'Hanlon *et al.*, Prognostic significance of myocardial fibrosis in hypertrophic cardiomyopathy. *J. Am. Coll. Cardiol.* **56**, 867–874 (2010).
11. M. Klopotowski *et al.*, The value of cardiac magnetic resonance and distribution of late gadolinium enhancement for risk stratification of sudden cardiac death in patients with hypertrophic cardiomyopathy. *J. Cardiol.* **68**, 49–56 (2016).
12. C. Y. Ho *et al.*, T1 measurements identify extracellular volume expansion in hypertrophic cardiomyopathy sarcomere mutation carriers with and without left ventricular hypertrophy. *Circ. Cardiovasc. Imaging* **6**, 415–422 (2013).
13. A. Axelsson Raja *et al.*, Prevalence and progression of late gadolinium enhancement in children and adolescents with hypertrophic cardiomyopathy. *Circulation* **138**, 782–792 (2018).
14. P. Teekakirikul *et al.*, Cardiac fibrosis in mice with hypertrophic cardiomyopathy is mediated by non-myocyte proliferation and requires Tgf-β. *J. Clin. Invest.* **120**, 3520–3529 (2010).
15. C. Y. Ho *et al.*, Myocardial fibrosis as an early manifestation of hypertrophic cardiomyopathy. *N. Engl. J. Med.* **363**, 552–563 (2010).
16. T. Tsoutsman *et al.*, CCN2 plays a key role in extracellular matrix gene expression in severe hypertrophic cardiomyopathy and heart failure. *J. Mol. Cell. Cardiol.* **62**, 164–178 (2013).
17. M. Litviňuková *et al.*, Cells of the adult human heart. *Nature* **588**, 466–472 (2020).
18. A. A. Geisterfer-Lowrance *et al.*, A mouse model of familial hypertrophic cardiomyopathy. *Science* **272**, 731–734 (1996).
19. J. Yang *et al.*, Lysophosphatidic acid is associated with cardiac dysfunction and hypertrophy by suppressing autophagy via the LPA3/AKT/mTOR pathway. *Front. Physiol.* **9**, 1315 (2018).
20. A. M. Tager *et al.*, The lysophosphatidic acid receptor LPA1 links pulmonary fibrosis to lung injury by mediating fibroblast recruitment and vascular leak. *Nat. Med.* **14**, 45–54 (2008).
21. M. Funke, Z. Zhao, Y. Xu, J. Chun, A. M. Tager, The lysophosphatidic acid receptor LPA1 promotes epithelial cell apoptosis after lung injury. *Am. J. Respir. Cell Mol. Biol.* **46**, 355–364 (2012).
22. N. Sakai *et al.*, Lysophosphatidic acid signaling through its receptor initiates profibrotic epithelial cell fibroblast communication mediated by epithelial cell derived connective tissue growth factor. *Kidney Int.* **91**, 628–641 (2017).
23. F. V. Castelino *et al.*, Amelioration of dermal fibrosis by genetic deletion or pharmacologic antagonism of lysophosphatidic acid receptor 1 in a mouse model of scleroderma. *Arthritis Rheum.* **63**, 1405–1415 (2011).
24. J. P. Pradère *et al.*, LPA1 receptor activation promotes renal interstitial fibrosis. *J. Am. Soc. Nephrol.* **18**, 3110–3118 (2007).
25. S. Nakagawa *et al.*; Precision Liver Cancer Prevention Consortium, Molecular liver cancer prevention in cirrhosis by organ transcriptome analysis and lysophosphatidic acid pathway inhibition. *Cancer Cell* **30**, 879–890 (2016).
26. Y. Allanore *et al.*, Lysophosphatidic acid receptor 1 antagonist SAR100842 for patients with diffuse cutaneous systemic sclerosis: A double-blind, randomized, eight-week placebo-controlled study followed by a sixteen-week open-label extension study. *Arthritis Rheumatol.* **70**, 1634–1643 (2018).
27. S. M. Palmer *et al.*, Randomized, double-blind, placebo-controlled, phase 2 trial of BMS-986020, a lysophosphatidic acid receptor antagonist for the treatment of idiopathic pulmonary fibrosis. *Chest* **154**, 1061–1069 (2018).
28. D. Spiering, L. Hodgson, Dynamics of the Rho-family small GTPases in actin regulation and motility. *Cell Adhes. Migr.* **5**, 170–180 (2011).
29. Z. G. Ma, Y. P. Yuan, H. M. Wu, X. Zhang, Q. Z. Tang, Cardiac fibrosis: New insights into the pathogenesis. *Int. J. Biol. Sci.* **14**, 1645–1657 (2018).
30. X. Zhou *et al.*, Genomic differences distinguish the myofibroblast phenotype of distal lung fibroblasts from airway fibroblasts. *Am. J. Respir. Cell Mol. Biol.* **45**, 1256–1262 (2011).
31. R. Hilal-Dandan *et al.*, Lysophosphatidic acid induces hypertrophy of neonatal cardiac myocytes via activation of Gi and Rho. *J. Mol. Cell. Cardiol.* **36**, 481–493 (2004).
32. J. Chen *et al.*, Specific receptor subtype mediation of LPA-induced dual effects in cardiac fibroblasts. *FEBS Lett.* **580**, 4737–4745 (2006).
33. X. Chen *et al.*, Serum lysophosphatidic acid concentrations measured by dot immunogold filtration assay in patients with acute myocardial infarction. *Scand. J. Clin. Lab. Invest.* **63**, 497–503 (2003).
34. X. Liu *et al.*, Lymphoangiocrine signals promote cardiac growth and repair. *Nature* **588**, 705–711 (2020).
35. A. Botella-Lopez *et al.*, Reelin is overexpressed in the liver and plasma of bile duct ligated rats and its levels and glycosylation are altered in plasma of humans with cirrhosis. *Int. J. Biochem. Cell Biol.* **40**, 766–775 (2008).
36. S. Carotti *et al.*, Reelin expression in human liver of patients with chronic hepatitis C infection. *Eur. J. Histochem.* **61**, 2745 (2017).
37. Y. Ding *et al.*, Loss of Reelin protects against atherosclerosis by reducing leukocyte-endothelial cell adhesion and lesion macrophage accumulation. *Sci. Signal.* **9**, ra29 (2016).
38. I. Krueger *et al.*, Reelin amplifies glycoprotein VI activation and AlphaIIb Beta3 integrin outside-in signaling via PLC gamma 2 and Rho GTPases. *Arterioscler. Thromb. Vasc. Biol.* **40**, 2391–2403 (2020).
39. B. A. J. Tamburini *et al.*, Chronic liver disease in humans causes expansion and differentiation of liver lymphatic endothelial cells. *Front. Immunol.* **10**, 1036 (2019).
40. T. Ueland *et al.*; Investigators of the Controlled Rosuvastatin Multinational Study in Heart Failure (CORONA) trial; Investigators of the GISSI-Heart Failure (GISSI-HF) trial, CCL21 is associated with fatal outcomes in chronic heart failure: Data from CORONA and GISSI-HF trials. *Eur. J. Heart Fail.* **15**, 747–755 (2013).
41. A. Bonacchi *et al.*, The chemokine CCL21 modulates lymphocyte recruitment and fibrosis in chronic hepatitis C. *Gastroenterology* **125**, 1060–1076 (2003).
42. N. Sakai *et al.*, Secondary lymphoid tissue chemokine (SLC/CCL21)/CCR7 signaling regulates fibrocytes in renal fibrosis. *Proc. Natl. Acad. Sci. U.S.A.* **103**, 14098–14103 (2006).
43. G. Pei *et al.*, Lymphangiogenesis in kidney and lymph node mediates renal inflammation and fibrosis. *Sci. Adv.* **5**, eaaw5075 (2019).
44. C. K. Nagaraju *et al.*, Global fibroblast activation throughout the left ventricle but localized fibrosis after myocardial infarction. *Sci. Rep.* **7**, 10801 (2017).
45. H. Aghajanian *et al.*, Targeting cardiac fibrosis with engineered T cells. *Nature* **573**, 430–433 (2019).
46. J. J. Contos, N. Fukushima, J. A. Weiner, D. Kaushal, J. Chun, Requirement for the lpA1 lysophosphatidic acid receptor gene in normal suckling behavior. *Proc. Natl. Acad. Sci. U.S.A.* **97**, 13384–13389 (2000).
47. S. D. Solomon *et al.*, Familial hypertrophic cardiomyopathy is a genetically heterogeneous disease. *J. Clin. Invest.* **86**, 993–999 (1990).
48. E. M. Green *et al.*, A small-molecule inhibitor of sarcomere contractility suppresses hypertrophic cardiomyopathy in mice. *Science* **351**, 617–621 (2016).
49. W. Wan, L. Leinwand, Computational approach to measuring myocyte disarray in animal models of heart disease. *Curr. Protoc. Hum. Genet.* **93**, 15.11.1–15.11.9 (2017).
50. W. Wan, J. B. Dixon, R. L. Gleason Jr., Constitutive modeling of mouse carotid arteries using experimentally measured microstructural parameters. *Biophys. J.* **102**, 2916–2925 (2012).
51. D. C. Christodoulou *et al.*, 5'RNA-Seq identifies Fhl1 as a genetic modifier in cardiomyopathy. *J. Clin. Invest.* **124**, 1364–1370 (2014).
52. A. Dobin *et al.*, STAR: Ultrafast universal RNA-seq aligner. *Bioinformatics* **29**, 15–21 (2013).
53. E. R. Nadelmann *et al.*, Isolation of nuclei from mammalian cells and tissues for single-nucleus molecular profiling. *Curr. Protoc.* **1**, e132 (2021).
54. M. Litvinukova *et al.*, Single cell and single nuclei analysis human heart tissue. Protocols.io (2018). https://www.protocols.io/view/single-cell-and-single-nuclei-analysis-human-heart-x54v98pkml3e/v1. Accessed 14 June 2022.
55. T. Stuart *et al.*, Comprehensive integration of single-cell data. *Cell* **177**, 1888–1902.e21 (2019).
56. I. Korsunsky *et al.*, Fast, sensitive and accurate integration of single-cell data with Harmony. *Nat. Methods* **16**, 1289–1296 (2019).
57. J. Schindelin *et al.*, Fiji: An open-source platform for biological-image analysis. *Nat. Methods* **9**, 676–682 (2012).
58. A. Axelsson Raja, "Replication Data for: LPA-403." Harvard Dataverse. 10.7910/DVN/KXPFKK. Deposited 14 June 2022.